

Development of High-Speed Ion Conductance Microscopy

Shinji Watanabe,^{1,*} Satoko Kitazawa,² Linhao Sun,¹ Noriyuki Kodera,¹ and Toshio Ando^{1,†}

¹*WPI Nano Life Science Institute (WPI-NanoLSI),
Kanazawa University, Kakuma-machi, Kanazawa 920-1192, Japan*

²*Department of Physics, Institute of Science and Engineering,
Kanazawa University, Kakuma-machi, Kanazawa 920-1192, Japan*

(Dated: December 25, 2019)

Scanning ion conductance microscopy (SICM) can image the surface topography of specimens in ionic solutions without mechanical probe-sample contact. This unique capability is advantageous for imaging fragile biological samples but its highest possible imaging rate is far lower than the level desired in biological studies. Here, we present the development of high-speed SICM. The fast imaging capability is attained by a fast Z-scanner with active vibration control and pipette probes with enhanced ion conductance. By the former, the delay of probe Z-positioning is minimized to sub-10 μs , while its maximum stroke is secured at 6 μm . The enhanced ion conductance lowers a noise floor in ion current detection, increasing the detection bandwidth up to 100 kHz. Thus, temporal resolution 100-fold higher than that of conventional systems is achieved, together with spatial resolution around 20 nm.

I. INTRODUCTION

Tapping mode atomic force microscopy (AFM) [1] has been widely used to visualize biological samples in aqueous solution with high spatial resolution. However, when the sample is very soft, like eukaryotic cell surfaces, the intermittent tip-sample contact significantly deforms the sample and hence blurs its image [2–4]. Moreover, when the sample is extremely fragile, it is often seriously damaged [4, 5]. SICM was invented to overcome this problem [6]. SICM uses as a probe an electrolyte-filled pipette having a nanopore at the tip end, and measures an ion current that flows between an electrode inside the pipette and another electrode in the external bath solution. The ionic current resistance between the pipette tip and sample surface (referred to as the access resistance) increases when the tip approaches the sample. This sensitivity of access resistance to the tip-sample distance enables imaging of the sample surface without mechanical tip-sample contact [7, 8] (Fig. 1). To improve fundamental performances of SICM, several devices have recently been introduced, including a technique to control the pore size of pipettes [9–11] and a feedback control technique based on tip-sample distance modulation [12–14]. Moreover, the SICM nanopipette has recently been used to measure surface charge density [15–21] and electrochemical activity [22, 23] as well as to deliver species [24–27]. Thus, SICM is now becoming a useful tool in biological studies, especially for characterizing single cells with very soft and fragile surfaces [28].

However, the imaging speed of SICM is low; it takes from a few minutes to a few tens of minutes to capture an SICM image, which is in striking contrast to AFM. High-speed AFM is already established [29]

and has been used to observe a variety of proteins molecules and organelles in dynamic action [30]. The slow performance of SICM is due mainly to a low signal-to-noise ratio (SNR) of ion current sensing, resulting in its low detection bandwidth (and hence low feedback bandwidth). Moreover, the low resonant frequency of the Z-scanner also limits the feedback bandwidth.

When the vertical scan of the pipette towards the sample is performed with velocity v_z , the time delay of feedback control t_{delay} causes an overshoot for the vertical scan by $t_{\text{delay}} \times v_z$. This overshoot distance should be smaller than the closest tip-sample distance (d_c) to be maintained during imaging (see the approach curve in Fig. 1). That is,

$$v_z \leq \frac{d_c}{t_{\text{delay}}}. \quad (1)$$

An appropriate size of d_c is related to the pipette geometry, such as the tip aperture radius r_a , the cone angle θ_c , and the outer radius of the tip r_o [7, 31, 32], but $d_c \approx 2r_a$ is typically used to achieve highest possible resolution. The size of t_{delay} can be roughly estimated from the resonant frequency of the Z-scanner f_z and the bandwidth of ion current detection B_{id} , as $t_{\text{delay}} \approx 1/f_z + 1/B_{\text{id}}$. In typical SICM setups, the values of these parameters are $r_a \approx 20$ nm, $f_z \approx 1$ kHz and $B_{\text{id}} \approx 1$ kHz, yielding $v_z < 20$ $\mu\text{m/s}$. In the representative SICM imaging mode referred to as the hopping mode [33], the tip-approach and retract cycle is repeated for a distance (hopping amplitude) of slightly larger than the sample height, h_s . For example, when $v_z = 20$ $\mu\text{m/s}$ is used for the sample with $h_s \approx 1$ μm , it takes at least > 50 ms for pixel acquisition, which depends on the retraction speed. This pixel acquisition time corresponds to an imaging acquisition time longer than 8.3 min for 100×100 pixel resolution [34]. When the pipette retraction speed can be set at much larger than the approach speed v_z , the

* wshinji@se.kanazawa-u.ac.jp;

† tando@staff.kanazawa-u.ac.jp;

imaging acquisition time can be improved but not much.

Several groups have attempted to increase v_z [13, 34–38]. One of approaches used is to mount a shear piezoactuator with a high resonant frequency (but with a small stroke length) on the Z-scanner and this fast piezoactuator is used as a ‘brake booster’ [34, 35]; that is, this piezoactuator is activated only in the initial retraction phase where the tip is in close proximity to the surface. This method could cancel an overshooting displacement and therefore increase v_z by 10-fold. Another approach is to increase B_{id} by the improvement of the SNR of current signal detection with the use of a current-source amplification scheme [37] or by the use of AC bias voltage between the electrodes (the AC current in phase with the AC bias voltage is used as an input for feedback control) [13, 38]. This bias voltage modulation method is further improved by capacitance compensation [14]. The improvement of SICM speed performance by these methods is however limited to a few times at most. Very recently, two studies demonstrated fast imaging of live cells with the use of their high-speed SICM (HS-SICM) systems [39, 40]. However, one of these studies used temporal tip-sample contact to alter hopping amplitude [39], while the other used pipettes with $r_a = 80\text{--}100\text{ nm}$ and abandoned optical observation of the sample [40]. Note that in SICM the temporal resolution has a trade-off relationship with the spatial resolution, as in the cases of other measurement techniques. Thus far, no attempts have been made to increase both f_z and B_{id} extensively, without compromise of the spatial resolution and non-contact imaging capability of SICM.

Here, we report the development of HS-SICM and demonstrate its high-speed and high resolution imaging capability. The image rate was improved by a factor of ~ 100 or slightly more. This remarkable enhancement in speed was achieved by two improved performances: (i) fast pipette positioning achieved with the developed fast scanner and vibration suppression techniques and (ii) an enhanced SNR of current detection by reduction of the ionic resistance arising from the inside of the pipette (referred to as the pipette resistance). The improved f_z of the Z-scanner resulted in a mechanical response time of $\sim 3\mu\text{s}$, corresponding to a ~ 100 -fold improvement over conventional SICM systems. The SNR of current detection was improved by a factor of ~ 8 , enhancing B_{id} from 1 to 100 kHz or slightly higher. The HS-SICM system was demonstrated to be able to capture topographic images of low-height biological samples at 0.9–5 s/frame and live cells at 20–28 s/frame. These high imaging rate performances are compatible with spatial resolution of 15–23 nm.

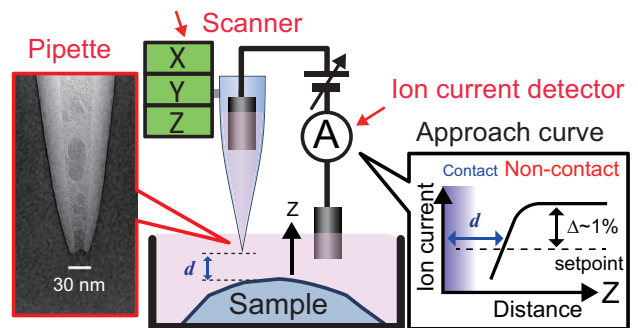


FIG. 1. Working principle of SICM. The electrolyte-filled pipette with a nanopore at its end (see the transmission electron micrograph in the left panel) is mounted on the scanner. The ion current through the nanopore generated by the application of bias voltage between the two Ag/AgCl electrodes is measured by the ion current detector. The measured ion current, which is dependent on the tip–surface separation d , is used as a pipette Z-position control signal.

II. RESULTS AND DISCUSSION

A. Strategy towards HS-SICM

The speed of pipette approach towards the sample (v_z) is limited, as expressed by Eq. (1). As v_z depends on f_z and B_{id} , the improvement on both f_z and B_{id} is required to achieve HS-SICM. To increase f_z , we need a fast Z-scanner for displacing the pipette along its length. Note that all commercially available Z-scanners for SICM have $f_z < 10\text{ kHz}$. Besides, we need to establish a method to mount the pipette ($\sim 15\text{ mm}$ in length) to the Z-scanner in order to minimize the generation of undesirable vibrations of the pipette. We previously developed a fast XYZ scanner with $f_z \approx 100\text{ kHz}$, a resonant frequency of $\sim 2.3\text{ kHz}$ in the XY directions, and stroke distances of $\sim 6\mu\text{m}$ and $\sim 34\mu\text{m}$ for Z and XY, respectively [41]. In this study, we further improved the dynamic response of this fast scanner. Considering this high f_z with improved dynamic response, we need to increase B_{id} to the level of $\sim 100\text{ kHz}$. As the ion current change caused by an altered tip-sample distance is generally small ($\sim 1\text{ pA}$), the current signal noise largely limits B_{id} . At a high frequency regime ($> 10\text{ kHz}$), the dominant noise source is the interaction between the amplifier’s current noise and the total capacitance at the input [42–44]. Therefore, we have to lower the total capacitance and increase the current signal to achieve $B_{id} \approx 100\text{ kHz}$, without increasing the pipette pore size.

B. High-speed Z-scanner

The structure of our fast scanner developed is shown in Fig. 2a-c. A key mechanism for minimizing unwanted Z-scanner vibrations is momentum cancellation; the hollow Z-piezoactuator is sandwiched with a pair of

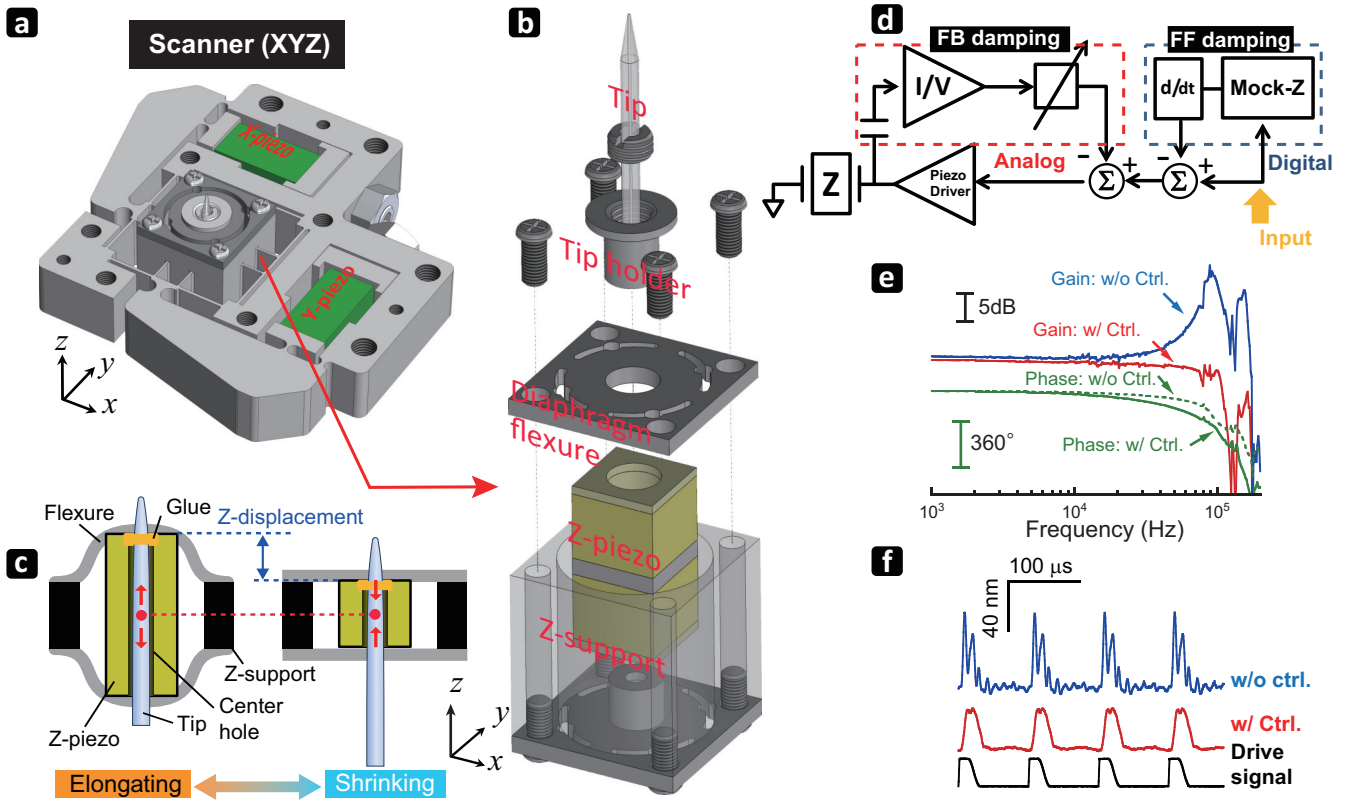


FIG. 2. XYZ-scanner used in this study. (a) Assembly drawing of the scanner. For the lateral scan, the displacements of X- and Y-piezoactuators are magnified via a lever arm amplification scheme. (b) Exploded view of the Z-scanner. (c) Assembly drawing showing the inertia balance design used for the Z-scanner. (d) Schematic of FF and FB damping control methods. (e) Transfer functions (frequency response) of Z-scanner. The blue and red lines indicate the gain signals measured without and with the damping control methods, respectively. The green broken and solid lines indicate the phase signals measured without and with the damping control methods, respectively. (f) Time domain responses of the Z-scanner in the application of a square-like waveform voltage to the input (black line). The blue and red lines show the measured Z-scanner displacements without and with the use of the damping control methods, respectively.

identical diaphragm-like flexures, so that the center of mass of the Z-piezoactuator hardly changes during its fast displacement (Supplementary material, SI 1). The pipette is mechanically connected only with the top flexure through being glued to the top clamp. Thanks to these designs, no noticeable resonance peaks are induced except at the resonant frequency of the Z-piezoactuator (Fig. 2e). We achieved a product value of $6\ \mu\text{m}$ (maximum displacement) \times $100\ \text{kHz}$ (resonant frequency) in this Z-scanner, which exceeds more than 10-fold the value of conventional designs of SICM Z-scanner, $25\ \mu\text{m} \times 1\text{--}2\ \text{kHz}$. In the present study, we further improved the dynamic response of Z-scanner. The sharp resonant peak shown in Fig. 2e (blue line) induces unwanted vibrations. In fact, the application of a square-like-waveform voltage to the Z-scanner (black line in Fig. 2f) generated an undesirable ringing displacement of the Z-scanner (blue line in Fig. 2f). To damp this ringing, we developed feedforward (FF) and feedback (FB) control methods (Fig. 2d). The FF control system was implemented

in field-programmable-gate-array (FPGA). The gain controlled output signal from a mock Z-scanner (an electric circuit) with a transfer function similar to that of the real Z-scanner was first differentiated and then subtracted from the signal input to the Z-piezodriver [45]. Although this method was effective in reducing the Q-factor of the Z-scanner, the drift behavior of the transfer function of real Z-scanner would affect the reduced Q-factor during long-term scanning. To suppress the drift effect, the FB control implemented in an analog circuit was added as follows. The velocity of Z-scanner displacement was measured using the transimpedance amplifier via a small capacitor of $\sim 1\ \text{pF}$ positioned near the Z-scanner. The gain-controlled velocity signal was subtracted from the output of the FF controller. In this way, too fast movement of the Z-scanner was prevented [46], resulting in nearly complete damping of unwanted vibrations, as shown with the red lines of Figs. 2e and 2f. Thus, the open-loop response time of Z-scanner, $Q/\pi f_z$, was improved from $\sim 18.5\ \mu\text{s}$ to $1.8\ \mu\text{s}$ (critical damping). Note that measured Z-scanner

displacements (blue and red lines) include the latency of the laser vibrometer used ($2\ \mu\text{s}$) (Supplementary material, SI 1, Fig. S2). The FF/FB damping control was also applied to the XY scanners to improve their dynamic response (Supplementary material, SI 1, Fig. S3).

C. Enhancement of SNR with Salt Concentration Gradient

We describe here a method to improve B_{id} by increasing the SNR of current signal sensing. In the frequency region $> 10\ \text{kHz}$, the dominant noise source of the ion current detector is the total capacitance at the transimpedance amplifier input, ΣC [42, 43]:

$$I_{\text{RMS}} \propto B_{\text{id}}^{3/2} \Sigma C, \quad (2)$$

where I_{RMS} represents a root-mean-square current noise. The electrode-wiring and the pipette capacitance C_p dominate the total capacitance. As the C_p derives from the part of the pipette immersed in solution, thicker wall pipettes are useful in reducing C_p . We used quartz capillaries with a wall thickness of $0.5\text{--}0.7\ \text{mm}$. The total capacitance in our setup was estimated to be $\sim 5\ \text{pF}$ (Supplementary material, SI 2), yielding $I_{\text{RMS}} \sim 8\ \text{pA}$ at $B_{\text{id}} = 100\ \text{kHz}$ (although I_{RMS} was $\sim 1.2\ \text{pA}$ at $B_{\text{id}} = 10\ \text{kHz}$), which was still too large. Then, we decided to increase the ion current to improve the SNR further. Since the bias voltage (V_b) larger than a typical value of $\pm 0.5\ \text{V}$ induces an unstable ion current [47], we need to reduce the pipette resistance (R_p). The ion current I_i through the pipette opening is approximately described as

$$I_i(d) = \frac{V_b}{R_a(d) + R_p}, \quad (3)$$

where d is the tip-surface distance and R_a is the access resistance that depends on d [48]. In Eq. 3, the surface charge-dependent ion current rectification in the pipette is not considered [49]. R_p is usually ~ 100 -times larger than R_a even at $d \approx d_c$, and therefore, the reduction of R_p directly increases I_i . To reduce R_p , we examined the ion concentration gradient (ICG) method; a pipette back-filled with a high salt solution is immersed in a low salt solution. Since the pipette opening is very small, a concentration gradient is expected to be formed only in the close vicinity of the pipette opening. Although several studies have been performed on ICG from the viewpoint of its effect on the ion current rectification in nanopores [50–52], it is unclear whether or not the ICG method is really useful and applicable to SICM, as the physiological salt concentration used in the external bath solutions is relatively high. To check this issue, we first performed a finite element method (FEM) simulation using the coupled Poisson–Nernst–Planck

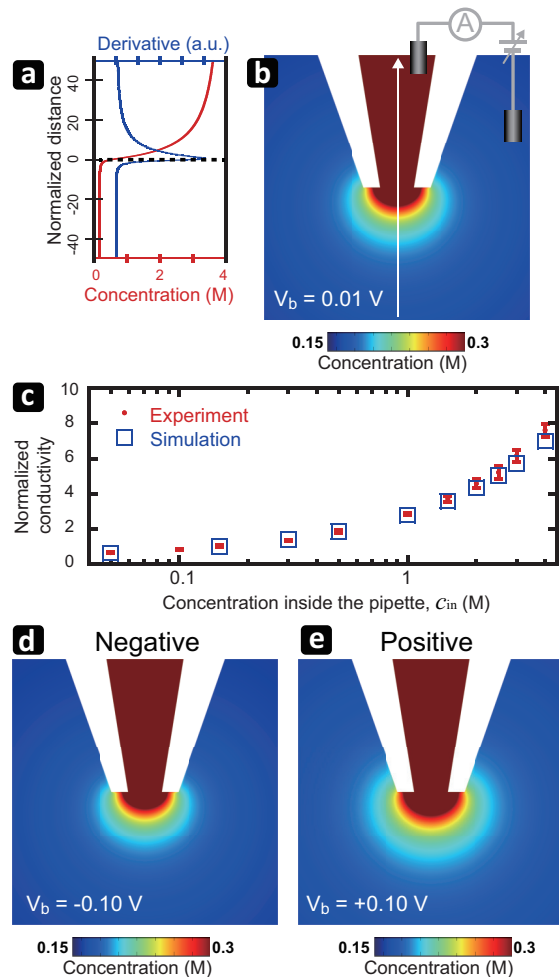


FIG. 3. Spatial distribution of average concentration of K^+ and Cl^- obtained by FEM simulation. The surface charge density of the tip was set at $-10\ \text{mC}/\text{m}^2$. (a) Average ion concentration profile (red) and its derivative (blue) along the white arrow shown in (b). c_{in} (KCl) = $4\ \text{M}$, c_{out} (KCl) = $0.15\ \text{M}$ and $V_b = 0.01\ \text{V}$ were used. The vertical axis represents the Z-distance from the tip aperture normalized with the tip aperture diameter; the tip aperture position is zero as indicated by the broken line. (b) Spatial distribution of average ion concentration under the same conditions as (a). (c) Enhancement of tip conductivity by ICG. The vertical axis represents the enhancement factor of the tip conductivity with respect to the ion conductivity at $c_{\text{in}} = 0.15\ \text{M}$. (d, e) Spatial distributions of average ion concentration at $V_b = -0.1\ \text{V}$ (d) and $V_b = 0.1\ \text{V}$ (e) for c_{in} (KCl) = $4\ \text{M}$ and c_{out} (KCl) = $0.15\ \text{M}$.

(PNP) equations that have been widely adopted to study the transport behavior of charged species [20, 53, 54]. Full details of our PNP simulation setup are described in Supplementary material, SI 3 and Methods. Figures 3a,b show a FEM simulation result obtained for the spatial profile of total ion concentration $(c_{\text{K}^+} + c_{\text{Cl}^-})/2$, when $4\ \text{M}$ KCl and physiological $0.15\ \text{M}$ KCl solutions were used for the inside and outside of the pipette, respectively. As seen there, the region of ICG is confined

in a small volume around the pipette opening, while the outside salt concentration is maintained at ~ 0.23 M and < 0.17 M in the regions distant from the opening by $\sim 2r_a$ and $> 4r_a$, respectively. Figure 3c (square plots) shows a simulation result for changes of ion conductance $1/R_p$ when the KCl concentration inside the pipette (c_{in}) was altered, while the outside bulk KCl concentration (c_{out}) was kept at 0.15 M. This result was very consistent with that obtained experimentally (red plots in Fig. 3c). The value of $1/R_p$ at $c_{in} = 4$ M was ~ 8 -times larger than that at $c_{in} = 0.15$ M. We also confirmed that the conditions of $c_{in} = 4$ M and $c_{out} = 0.15$ M generate a steady current with $|V_b| < 0.5$ V, and hence, allow stable SICM measurements for $7.5 \text{ nm} \leq r_a \leq 25 \text{ nm}$. Note that the high KCl concentration region can be confined to a smaller space when a negative bias voltage is used because of an ion current rectification effect of the negatively charged pipette (Fig. 3d, e).

To confirm the SNR enhancement of I_i by ICG formed by the use of $c_{in} = 4$ M and $c_{out} = 0.15$ M, we measured the dynamic responses of I_i to quick change of d under $V_b = 0.5$ V, in the presence and absence of ICG. To measure the responses, the pipette with $r_a = 10$ nm was initially positioned at a Z-point showing 5% reduction of I_i (see Fig. 4a). Then, the pipette was quickly retracted by 10 nm within 14 μs , and after a while quickly approached by 10 nm within 14 μs (Fig. 4b, Top), by the application of a driving signal with a rectangle-like waveform (Fig. 4b, Bottom) to the developed Z-scanner. The ion current responses measured using the transimpedance amplifier with $B_{id} = 400$ kHz are shown in Fig. 4b (Middle). With ICG, a clear response was observed (blue line), whereas without ICG no clear response was observed (red line) due to a large noise floor at this high bandwidth. With ICG, the SNR of detected current response increased linearly with increasing V_b (Fig. 4c, blue plots; [Supplementary material](#), SI 4, Fig. S8), although the instability of detected I_i was confirmed at $V_b > 0.5$ V (not shown). Thus, the SNR of current detection was ~ 8 times improved by the ICG method (Fig. 4c).

The rising and falling times of the measured current changes with ICG were indistinguishable from those of the piezodriver voltage (Fig. 4b, Middle and Bottom), indicating no noticeable delay ($< \sim 2$ μs) in the measured current response. Note that the physically occurring (not measured) response of current change (or the rearrangement of ion distribution) must be much faster than the response of measured current changes, because the actual response is governed by the local mass transport time in the nanospace around the pipette opening. The response time is roughly estimated to be 133 ns by adopting the diffusion time (τ) required for ion transport by a distance of $2r_a = 20$ nm: $2r_a = \sqrt{2D\tau}$, where D is the nearly identical diffusion coefficient of K^+ and Cl^- in water ($\sim 1.5 \times 10^{-9} \text{ m}^2/\text{s}$) [55].

Contrary to our expectation, the normalized approach curve (I_i vs d) was nearly identical between the pipettes

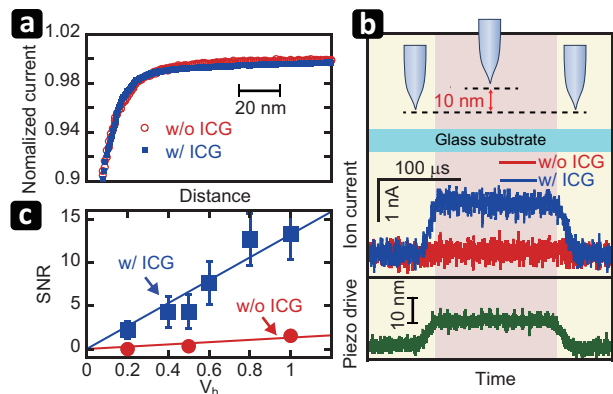


FIG. 4. Enhancement of ion current response by ICG. (a) Approach curves with (blue) and without (red) ICG method. (b) Dynamic response of ion current at $V_b = 0.5$ V when the tip is vertically moved (shown in green) in close proximity to the glass surface, and its dependence on the use (shown in blue) and non-use (shown in red) of ICG method. (c) Increase of SNR of ion current measurement with increasing V_b and its dependence on the use (blue) and non-use (red) of ICG method.

with and without ICG (Fig. 4a) although their R_p values were largely different. This indicates a nearly identical R_a/R_p ratio between the two cases. This result was confirmed by FEM simulations performed by the use of various surface charge densities of pipette and substrate in a range of 0–20 mC/m^2 ([Supplementary material](#), SI 5).

In the final part of this subsection, we considered how SICM measurements with ICG would affect the membrane potential of live cells in a physiological solution. The ICG modulates local ion concentrations around the pipette tip end, which might induce a change in the local membrane potential only when the tip is in the close vicinity to the cell surface. However, it is difficult to perform experimental measurements of such a transient change of the local membrane potential. Here we estimated this change for nonexcitable HeLa cells used in this study and typical excitable cells, using the Goldman-Hodgkin-Katz voltage equation [56, 57]. In this estimation, extracellular ion concentrations around the tip end were obtained by FEM simulations. Full details of this analysis are described in [Supplementary material](#), SI 3. For both cell types, we found that their local membrane potentials were changed by the pipette tip with ICG to various extents depending on the value of V_b (see [Supplementary material](#) SI 3, Tab. S3). However, for nonexcitable HeLa cell, we expect that the net contribution of an ICG-induced local membrane potential change is negligible as the tip pore size is very small. It may not be however negligible for excitable cells, because a local membrane potential change would trigger the opening of voltage-gated sodium ion channels and thus generate action potential, which would propagate over the cell membrane. A quantitative estimation

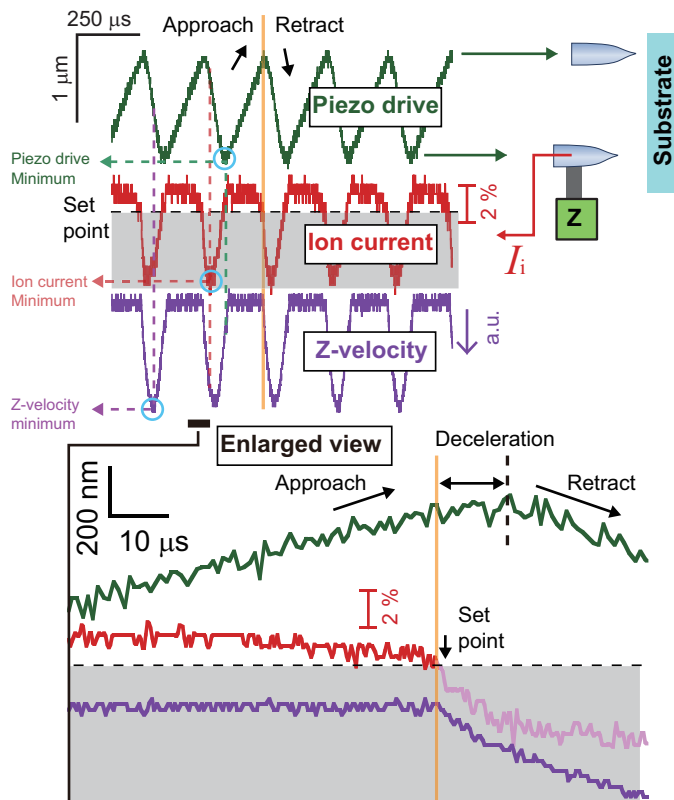


FIG. 5. Evaluation of improved approach velocity. The pipette tip was periodically moved in the z -direction, in close proximity to the glass substrate (right panel). (Left panel) The green line indicates the time course of tip displacement estimated from the Z-scanner’s drive voltage. The red line indicates the detected ion current signal. The purple line indicates the velocity of tip displacement estimated from the output current of the Z-piezodriver. (Bottom panel) An enlarged view showing these three quantities. The ion current signal in the shaded region (shown in pink) is a false one (mostly leakage current) caused by a capacitive coupling between the Z-piezoactuator and the signal line of ion current detection. A set point value of 2% was used.

for this possibility is beyond the scope of the present study. Nevertheless, our FEM simulations indicate that the ICG-induced local membrane potential change can be attenuated by the use of different V_b values and/or high concentration of NaCl solution instead of 4 M KCl solution (Supplementary material, SI 3, Tab. S4).

D. Evaluation of Improved v_z

Here we describe a quantitative evaluation of how significantly the pipette approach velocity is improved by the ICG method and the developed Z-scanner. Besides, we describe a problem we have encountered during this evaluation. For this evaluation, the pipette filled with 4 M KCl was vertically moved above the glass substrate in 0.15 M KCl solution (the Z-displacement and its velocity

are shown with the green and purple lines in Fig. 5, respectively), while the ion current was measured using the transimpedance amplifier with $B_{id} = 400$ kHz. For the initiation of $\sim 1.3 \mu\text{m}$ retraction of the pipette by feedback control, the set point of ion current was set at 98% of the reference ion current (i.e., 2% reduction). In the approaching regime, the ion current decreased as the tip got close proximity to the surface (red line in Fig. 5). However, in the retraction regime following the deceleration phase, the detected ion current behaved strangely; I_i initially decreased rather than increased and then reversed the changing direction, similar to the behavior of pipette Z-velocity (Supplementary material, SI 6, Fig. S10). We confirmed that this abnormal response of I_i was due to a leakage current caused by a capacitive coupling between the Z-piezoactuator and the signal line detecting I_i . We could mitigate this adverse effect by subtracting the gain-controlled Z-velocity signal from the measured I_i (Fig. S10). Although this abnormal response could not be completely cancelled as shown with the pink line in the shaded region of Fig. 5, it affected neither the feedback control nor SICM imaging. This is because the I_i signal in the retraction regime is not used in the operation of SICM. In the repeated approach and retraction experiments with the use of ICG method (Fig. 5), we achieved $v_z = 7.3 \mu\text{m}/\text{ms}$ for $r_a = 25$ nm, corresponding to 63% of the value estimated as $2 \times 25 \text{ nm}/[1.8 \mu\text{s} + (400 \text{ kHz})^{-1}] = 11.6 \mu\text{m}/\text{ms}$. This v_z value attained here is more than 300 times improvement over the v_z value used in a recent SICM imaging study on biological samples ($50 \text{ nm}/\text{ms}$ for $r_a = 50$ nm) with a conventional design of SICM Z-scanner [34]. Very recently, the Schäffer group successfully increased v_z up to $4.8 \mu\text{m}/\text{ms}$ for $r_a = 80\text{--}100$ nm using their sample stage scanner and a step retraction sequence called ‘turn step’ [40]. Our v_z value achieved for even 3–4 times smaller r_a still surpasses their result. We emphasize that the leakage of high salt to the outside of the tip is too small to change the bulk concentrations of ions outside and inside the tip. In addition, the region of ICG is confined to the vicinity of the tip for V_b values ($V_b \leq |0.1 \text{ V}|$) typically used in SICM measurements (Figs. 3d, e), and therefore, the sample remains in the bath salt condition most of time as the time when the sample stays within a distance of $\sim 2 \times r_a$ from the tip opening is very short ($\sim 10 \mu\text{s}$).

E. High-Speed Imaging of Grating Patterns

We evaluated the performance of our HS-SICM system by capturing topographic images of a sample made of polydimethylsiloxane that had a periodic $5 \times 5 \mu\text{m}^2$ checkerboard pattern with a height step of 100 nm (Grating 1). For this imaging in hopping mode, we used $r_a = 5\text{--}7.5$ nm and $B_{id} = 100$ kHz, values smaller than those used in the above evaluation test. Therefore, we reduced v_z to $150\text{--}550$ nm/ms. Other imaging conditions

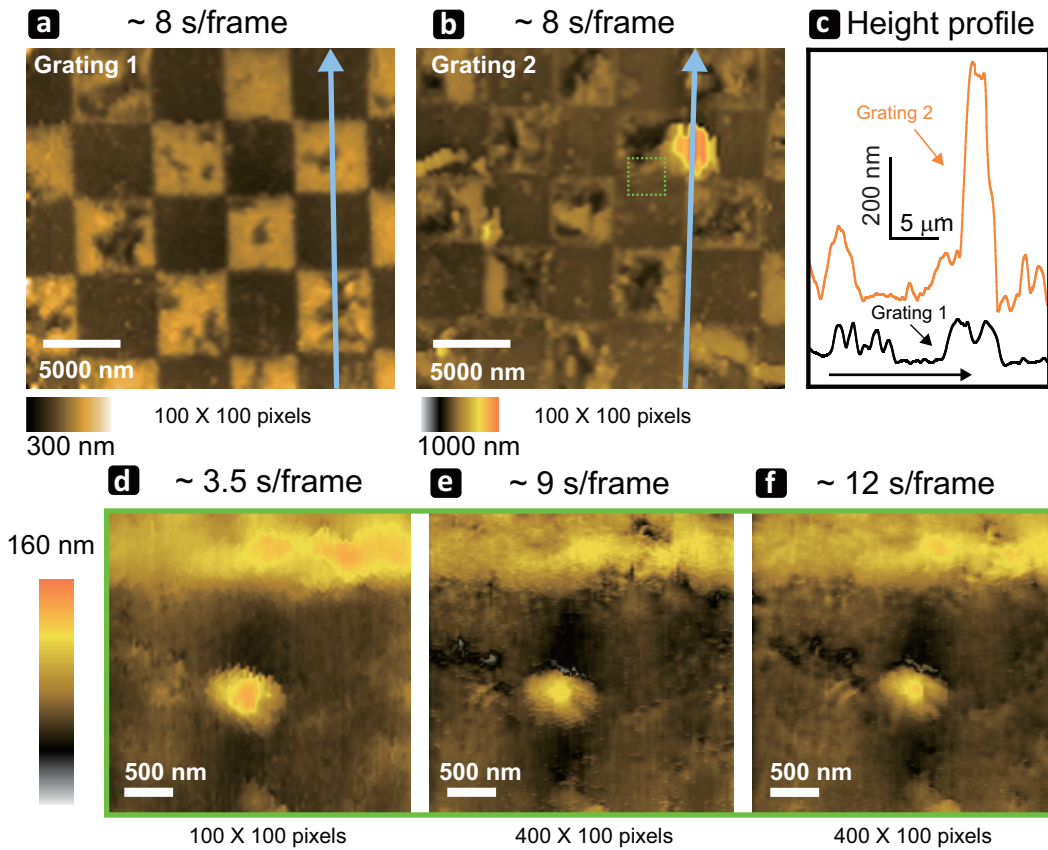


FIG. 6. HS-SICM images captured for grating samples. (a, b) Areas of $25 \times 25 \mu\text{m}^2$ were imaged at ~ 8 s/frame with 100×100 pixels for Grating 1 (a) and Grating 2 with a rougher surface (b). (c) Height profiles of Grating 1 and Grating 2 along the arrows shown in (a) and (b). (d–f) Images of the region shown with the small rectangle in (b) captured at ~ 3.5 (d), ~ 8.5 (e) and ~ 12 s/frame (f). A set point value of 2% was used to capture these images. The fast scan direction is from bottom to top in these imaging experiments.

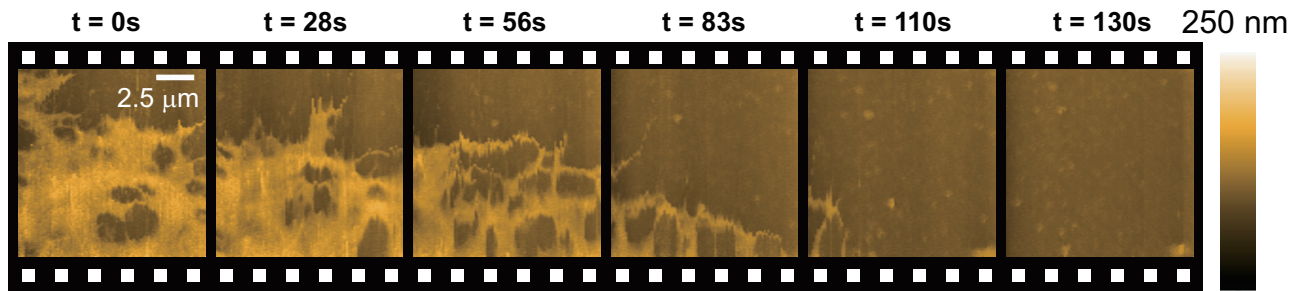


FIG. 7. Topographic images of edge region of HeLa cell on glass substrate successively captured at 20–28 s/frame with 200×100 pixels, under a pixel rate of 650–1000 Hz, hopping amplitude of 300–500 nm and $V_b = -0.1$ V. A set point value of 1.5% was used. The fast and slow scanning directions are from bottom to top and from left to right, respectively.

are $V_b = -0.3$ V and number of pixels = $100\text{--}400 \times 100$. Figure 6a shows a topographic image of Grating 1 captured at 8 s/frame over a $25 \times 25 \mu\text{m}^2$ area with 100×100 pixels. Figure 6b shows a topographic image of a rougher surface area of another grating sample (Grating 2) containing an object with a height of ~ 500 nm (Fig. 6c). Even for this rougher surface, its imaging was possible at 8 s/frame. Figures 6d–f show

images of a narrower area of Grating 2 marked with the small rectangle in Fig. 6b, captured at 3.5, 9 and 12 s/frame, respectively. Although fine structures were more visible in the images captured at 9 and 12 s/frame, this difference was not due to the lower imaging rates but due to the larger number of pixels. Averaged pixel rates were 2.85, 4.44 and 3.33 kHz for Figs. 6d, e and f, respectively, demonstrating high temporal and spatial

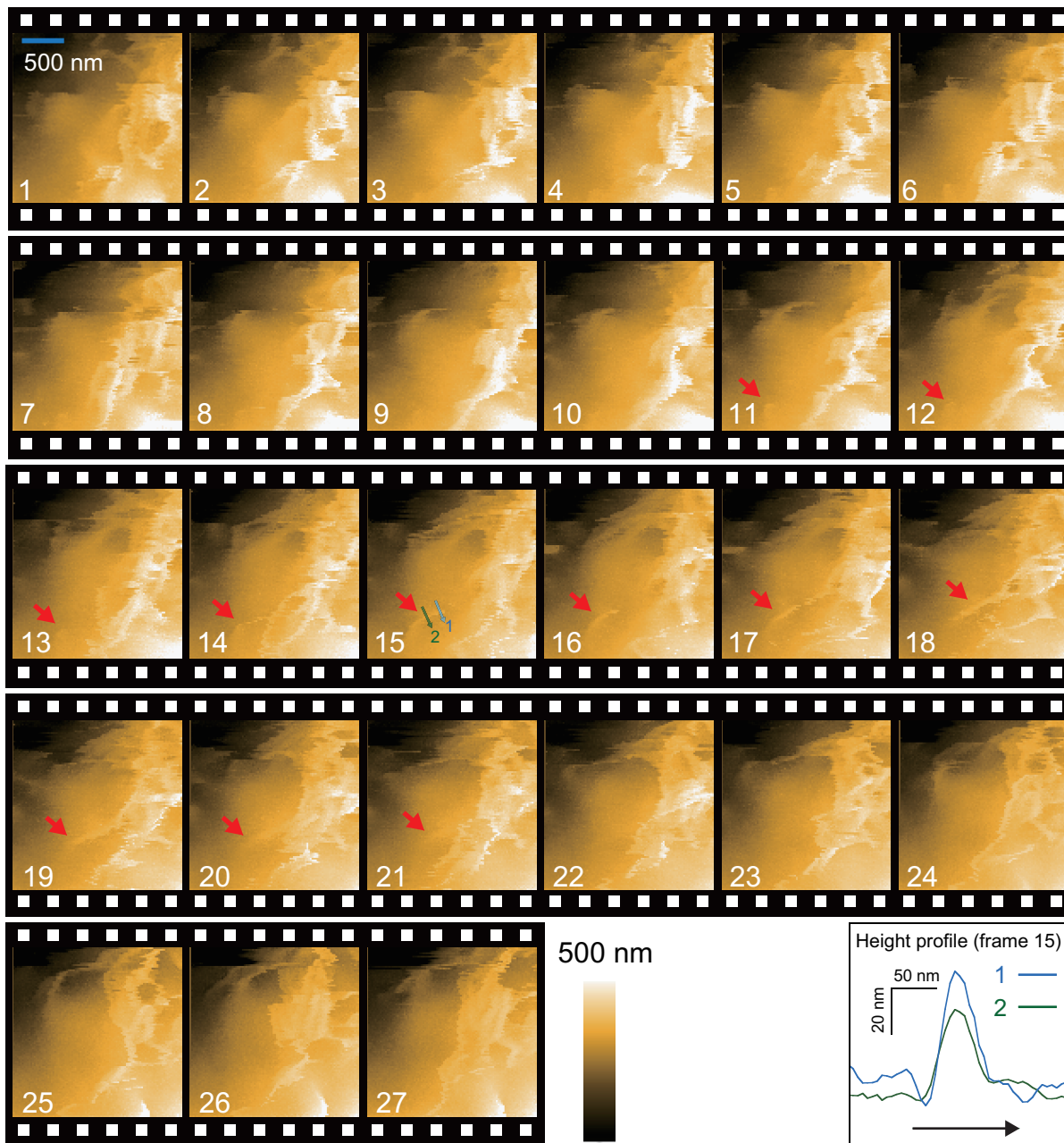


FIG. 8. Topographic images of microvilli dynamics on HeLa cell captured with HS-SICM. These images were successively captured at ~ 22 s/frame with 100×100 pixels, under a pixel rate of 455 Hz, hopping amplitude of 500–600 nm and $V_b = -0.2$ V. The numbers shown in each frame are the frame number. The red arrows indicate a microvillus undergoing growth and disappearance. The bottom right figure indicates the height profiles along the blue (1) and green (2) arrows shown in the frame 15. A set point value of 1% was used to capture these HS-SICM images. The fast and slow scanning directions are from left to right and from bottom to top, respectively.

resolution of our HS-SICM. Note that the imaging rate depends not only on v_z and a number of pixels but also on the hopping amplitude, hopping rate and the performance of the lateral movement of our scanner. In [Supplementary material](#), Fig. S11, we show examples of images captured at higher rates (~ 4 and ~ 0.3 s/frame).

F. High-Speed Imaging of Biological Samples

Next, we examined the applicability of our HS-SICM system to biological samples. The first test sample is a live HeLa human cervical cancer cell. The imaging was carried out in hopping mode using a pipette with $r_a = 5\text{--}7.5$ nm, $B_{id} = 100$ kHz and $V_b = -0.1$ V. Figure 7 shows topographic images of a peripheral edge region of a

HeLa cell locomoting on a glass substrate in a phosphate buffer saline, captured at 20–28 s/frame with 200×100 pixels for a scan area of $12 \times 12 \mu\text{m}^2$. During the overall locomotion downwards until the cell disappearance from the imaging area within 2 min, the sheet-like structures (lamellipodia) with ~ 100 nm height were observed to grow and retract. In this imaging, the pixel rate was 670–1000 Hz, making a large contrast with the pixel rate of ~ 70 Hz used in previous hopping-mode-SICM imaging of live cells without significant surface roughness [34, 35]. Additional HS-SICM images capturing the movement of a HeLa cell in a peripheral edge region are provided in Figs. S12 and S13 (Supplementary material, SI 7). Bright-field optical microscope images before and after these SICM measurements are also provided in Fig. S14. In these imaging experiments, $r_a = 2\text{--}3$ nm, $B_{\text{id}} = 20$ kHz, $V_b = 70$ mV, pixel rate = 250 Hz, and hopping amplitude = 350 nm are used.

To demonstrate the applicability of our HS-SICM system also to live cells with significant surface roughness, we next imaged a central region ($2 \times 2 \mu\text{m}^2$) of a HeLa cell at 22 s/frame, using pipettes with $r_a = 5\text{--}7.5$ nm, $B_{\text{id}} = 100$ kHz, $V_b = -0.2$ V, and hopping amplitude of 600 nm (Fig. 8 and Supplementary Movie 1). The captured images show moving, growing and retracting microvilli with straight-shaped and ridge-like structures [5, 39, 58]. The red arrows on frames 11–21 in Fig. 8 indicate the formation and disappearance of a single microvillus. During this dynamic process captured with a pixel rate of 0.56 kHz, the full width at half maximum (FWHM) of the microvillus was less than 50 nm (lower right in Fig. 8), when it was analyzed for the frame 15 (FWHM values of trace 1 and 2 are 38.8 ± 10.2 nm and 42.3 ± 10.2 nm, respectively). These values are less than the single pixel resolution in previous SICM measurements (100–200 nm) [5, 39]. As demonstrated here, we can get SICM images with higher spatial resolution without sacrificing the temporal resolution, as shown in Table 1 (compare the values of pixel rate and r_a among the three studies with respective HS-SICM systems developed).

In Figs. 7 and 8, slight discontinuities of images appear as noises between adjacent fast scan lines. In contrast, there are no such discontinuities in the images of stationary grating samples (Fig. 6a) captured with an even higher imaging rate than those used in Figs. 7 and 8. Moreover, during these imaging experiments, significant ion current reductions that could be caused by tip-sample contact [39] were not observed. Therefore, we speculate that the image discontinuities appeared in the images of live HeLa cells are due to autonomous movement of the cells and the small pipette aperture; small movements of HeLa cells that cannot be detected with a large aperture pipette ($r_a \sim 100$ nm) appear in our high resolution images.

Next, we performed HS-SICM imaging of actin filaments of ~ 7 nm in diameter, under the conditions of $r_a = 5\text{--}7.5$ nm, $B_{\text{id}} = 100$ kHz, $V_b = -0.2$ V,

pixel rate of 556–2000 Hz, and hopping amplitude of 100–250 nm. Figure 9a shows a topographic image captured at ~ 5 s/frame of an actin filament specimen placed on a glass substrate coated with positively charged aminopropyl-triethoxysilane. Figure 9b shows its enlarged image for the area shown with the red rectangle in Fig. 9a. The image exhibited a height variation along the filament, as indicated in Figs. 9c and d. The measured height obtained from the arrow position 3 is ~ 7 nm. However, the measured heights obtained from the arrow positions 1, 2, 4, 5, and 6 were around 14 nm. These results may indicate that the specimen partly contains vertically stacked two actin filaments. The measured FWHM was 38.1 ± 4.2 nm for the arrow position 3. This value is 5 times larger than the diameter of an actin filament. This result can be explained by the side wall effect [60]; the tip wall thickness, i.e., $r_o - r_i$, would expand the diameter of a small object measured with SICM [59]. The side wall effect also explains that the measured FWHMs for the arrow positions 1 (66.0 ± 2.6 nm) and 2 (50.6 ± 3.7 nm) were larger than that for the arrow position 3. Despite the pixel size of $8 \times 8 \text{ nm}^2$, the 36 nm crossover repeat of the two-stranded actin helix could not be resolved. This is not due to insufficient vertical resolution but due to insufficient lateral resolution of the pipette used.

Next, we used mica-supported neutral lipid bilayers containing biotin-lipid, instead of using the amino silane-coated glass substrate to avoid possible bundling of actin filaments on the positively charged surface. Figures 9e, f show images captured at 18 s/frame for partially biotinylated actin filaments immobilized on the lipid bilayers through streptavidin molecules with a low surface density. Measured heights of these filaments were $\sim 6\text{--}7$ nm (Figs. 9g and h). However, the measured height of the lipid bilayer was ~ 13 nm from the mica surface (Fig. 9), much larger than the bilayer thickness of ~ 5 nm [61]. This large measured thickness is possibly due to a sensitivity of I_t to negative charges on the mica surface [15, 19–21]. The surface charges of objects can change d_c even at constant V_b and constant set point [20], which can provide measured height largely deviating from real one. In the high resolution image of immobilized filaments (Fig. 9f), the measured value of FWHM was 33.3 ± 6.0 nm (Fig. 9h).

As demonstrated here, our HS-SICM enables fast imaging of molecules without sacrificing the pixel resolution, unlike previous works [34, 35]. When the number of pixels was reduced to 50×50 , we could achieve sub-second imaging for a low-height sample. Supplementary Movie 2 captured at 0.9 s/frame with 50×50 pixels over a $0.8 \times 0.8 \mu\text{m}^2$ area shows high fluidity-driven morphological changes of polymers formed from a silane coupling agent placed on mica.

TABLE 1. Comparison between three HS-SICM systems used for live cell imaging. The pixel rate is calculated by dividing the imaging rate by the number of pixels. r_a indicates the aperture radii of the pipettes used to obtain SICM images. The attainable spatial resolution of SICM can be roughly estimated as $3 \times r_a$ [59]. PRDA is defined as pixel rate divided by r_a .

Observation	Image rate (s/frame)	Pixel rate (s^{-1})	r_a (nm)	PRDA ($s^{-1}nm^{-1}$)	Reference
Endocytosis	6	68	50	1.4	Shevchuk et al. [35]
Exocytosis					
Peripheral edge	0.6	1707	80–100	17–21	Simeonov and Schäffer [40]
Peripheral edge	20–28	714–1000	5–7.5	95–200	This work
Microvilli	18	228	50–100	2.3–4.6	Ida et al. [39]
Microvilli	1.4	2926	80–100	29.3–36.6	Simeonov and Schäffer [40]
Microvilli	20	455	5–7.5	60.7–91.0	This work

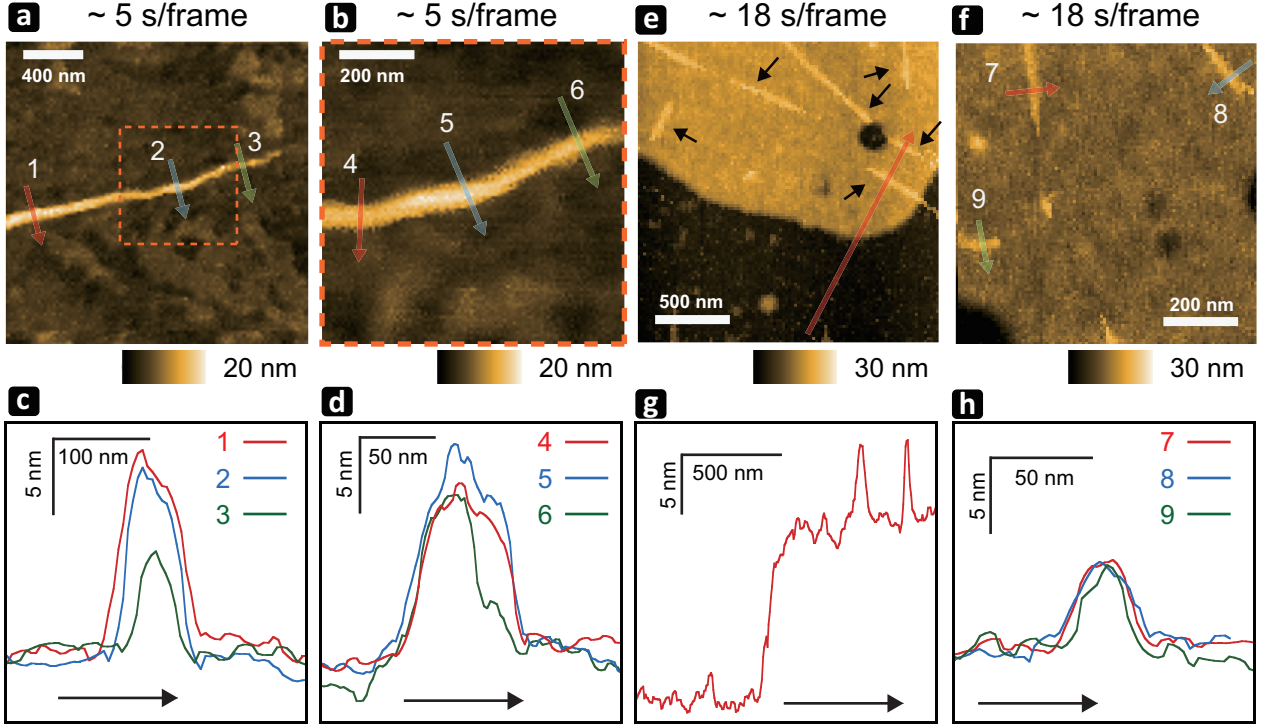


FIG. 9. HS-SICM images of actin filaments. (a–d) Actin filaments were attached onto a glass surface coated with positively charged amino-propyltriethoxysilane. (e–h) Partially biotinylated actin filaments were attached onto a mica-supported lipid bilayer containing a biotin-lipid through streptavidin molecules with a low surface density. (a) HS-SICM image captured at ~ 5 s/frame with 100×100 pixels, a pixel rate of 2000 Hz, hopping amplitude of 100 nm and $V_b = -0.2$ V. (b) A magnified view of the rectangle area shown in (a). (c) Height profiles along the arrows shown in (a). (d) Height profiles along the arrows shown in (b). (e, f) HS-SICM images captured at ~ 18 s/frame with 100×100 pixels, a pixel rate of 556 Hz, hopping amplitude of 250 nm and $V_b = -0.2$ V. (g) Height profile along the arrow shown in (e). (h) Height profiles along the arrows shown in (f). A set point value of 1.5% was used to capture these HS-SICM images.

G. Outlook for Higher Spatiotemporal Resolution

Finally, we discuss further possible improvements of HS-SICM towards higher spatiotemporal resolution. The speed performance of SICM can be represented by the value of pixel rate divided by r_a (we abbreviate this quantity as PRDA), because of a trade-off relationship between temporal resolution and spatial resolution. In Table 1, PRDA values of our HS-SICM imaging are shown, together with those of HS-SICM imaging in other labs. Although PRDA depends on sample height,

our HS-SICM system set a highest record, $PRDA = 95\text{--}200$ Hz/nm, in the imaging of a peripheral edge region of a HeLa cell. This record was attained by two means: the ICG method granting the high SNR of current detection and the high resonance frequency of the Z-scanner. Since we have not yet introduced other devices proposed previously for increasing the temporal resolution, there are still room for further speed enhancement. One of candidates to be added is (i) the ‘turn step’ procedure (applying a step function to the Z-piezodriver) developed by Simeonov and Schäffer for rapid pipette retraction [40]. Other candidates

would be (ii) further current noise reduction of the transimpedance amplifier in a high frequency region, and (iii) lock-in detection of AC current produced by modulation of the pipette Z-position with small amplitude [12]. Since our Z-scanner has a much higher resonance frequency than ever before, we will be able to use high-frequency modulation (~ 100 kHz) to achieve faster lock-in detection of AC current. For higher spatial resolution, we need to explore methods to fabricate a pipette with smaller r_a and r_o , without significantly increasing R_p . One of possibilities would be the use of a short carbon nanotube inserted to the nanopore of a glass pipette with low R_p .

III. CONCLUSIONS

HS-SICM has been desired to be established not only to improve the time efficiency of imaging but also to make it possible to visualize dynamic biological processes occurring in very soft, fragile or suspended (not on a substrate) samples that cannot be imaged with HS-AFM. As demonstrated in this study, the fast imaging capability of SICM can be achieved by the improvement of speed performances of pipette Z-positioning and ion current detection. The former was attained by the new Z-scanner and implementation of vibration damping techniques to the Z-scanner. The latter was attained by the minimization of the total capacitance at the amplifier input and by the reduction of R_p achieved with the ICG method, resulting in an increased SNR of ion current detection. The resulting v_z reached $0.55 \mu\text{m/ms}$ for $r_a = 5\text{--}7.5$ nm and $7.3 \mu\text{m/ms}$ for $r_a = 25$ nm. The value of $7.3 \mu\text{m/ms}$ is larger than the recent fastest record achieved by Simeonov and Schäffer: $4.8 \mu\text{m/ms}$ for $r_a = 80\text{--}100$ nm. Consequently, the highest possible imaging rate was enhanced by ~ 100 -times, compared to conventional SICM systems. Even sub-second imaging is now possible for a scan area of $0.8 \times 0.8 \mu\text{m}^2$ with 50×50 pixels, without compromise of spatial resolution. The achieved speed performance will contribute to the significant extension of SICM application in biological studies.

IV. METHODS

A. Fabrication of Nanopipettes

We prepared pipettes by pulling laser-heated quartz glass capillaries, QF100-70-7.5 (outer diameter, 1.0 mm; inner diameter, 0.50 mm; with filament) and Q100-30-15 (outer diameter, 1.0 mm; inner diameter, 0.30 mm; without filament) from Sutter Instrument, using a laser puller (Sutter Instrument, P-2000). Just before pulling, we softly plasma-etched for 5 min at 20 W under oxygen gas flow (120 mTorr), using a plasma etcher (South Bay Technology, PE2000) to remove unwanted

contamination inside the pipette. The size and cone angle of each pipette tip were estimated from its scanning electron micrographs (Zeiss, SUPRA 40VP), transmission electron micrographs (JOEL, JEM-2000EX), and measured electrical resistance. Pipettes prepared from QF100-70-7.5 were used for the conductance measurement shown in Fig. 3c.

B. Measurements of Z-scanner Transfer Function and Time Domain Response

The Z-scanner displacement was measured with a laser vibrometer (Polytech, NLV-2500 or Iwatsu, ST-3761). The transfer function characterizing the Z-scanner response was obtained using a network analyzer (Agilent Technology, E5106B). A square-like-waveform voltage generated with a function generator (NF Corp., WF1948) and then amplified with a piezodriver (MESTECK, M-2141; gain, $\times 15$; bandwidth, 1 MHz) was used for the measurement of time domain response of the Z-scanner.

C. Measurement of Pipette Conductance with and without ICG

To evaluate the enhancement of pipette conductance ($1/R_p$) by ICG, we prepared a pair of pipettes simultaneously produced from one pulled capillary, which exhibited a difference in r_a less than $\pm 10\%$, as confirmed by electrical conductance measurements under an identical condition. One of the pair of pipettes was applied to a conductance measurement under ICG, while the other to a conductance measurement without ICG. To obtain each plot in Fig. 3c, we measured ($1/R_p$) for more than 5 sets of pipettes. To avoid the non-linear current-potential problem arising from an ion current rectification effect, we used V_b ranging between -10 mV and 10 mV.

D. Measurements of Approach Curves and Response of Ion Current

To obtain the approach curves (I_i vs d) shown in Fig. 4a, a digital 6th-order low-pass filter was used with a cutoff frequency of 10 kHz. After the measurement of each curve under $V_b = 0.1$ V, the pipette was moved to a Z-position where the ion current reduction by 5% had been detected in the approach curve just obtained. Next, the cut-off frequency of the low-pass filter was increased to 400 kHz for the measurement of fast ion current response and V_b was set at a measurement value. Then, the experiment shown in Fig. 4b was performed. This series of measurements were repeated under different values of V_b and with/without ICG. The identical pipette was used through the experiments to remove variations that would arise from varied pipette

shapes. After completing the experiments without ICG, the KCl solution inside the pipette was replaced with a 4 M KCl solution by being immersed the pipette in a 4 M KCl solution for a sufficiently long time (> 60 min). The R_p value of the pipetted with ICG prepared in this way was confirmed to be nearly identical to that of a similar pipette filled with a 4 M KCl solution from the beginning.

E. HS-SICM Apparatus

The HS-SICM apparatus used in this study was controlled with home-written software built with Lab-view 2015 (National Instruments), which was also used for data acquisition and analysis. The HS-SICM imaging head includes the XYZ-scanner composed of AE0505D08D-H0F and AE0505D08DF piezoactuators for the Z and XY directions (both NEC/tokin), respectively, as shown in Fig. 2a. The Z- and XY-piezoactuators were driven using M-2141 and M-26110-2-K piezodrivers (both MESTEK), respectively. The overall control of the imaging head was performed with a home-written FPGA-based system (NI-5782 and NI-5781 with NI PXI-7954R for the Z- and XY-position control, respectively; all National Instruments). For coarse Z-positioning, the imaging head was vertically moved with an MTS25-Z8 stepping-motor-based linear stage (travel range, 25 mm; THORLABS). For the FF control, FPGA-integrated circuits were used, while homemade analog circuitries were used for FB and noise filtering. The sample was placed onto the home-built XY-coarse positioner with a travel range of 20 mm, which was placed onto an ECLIPSE Ti-U inverted optical microscope (Nikon). The ion current through the tip nanopore was detected via transimpedance amplifiers CA656F2 (bandwidth, 100 kHz; NF) and LCA-400K-10M (bandwidth, 400 kHz; FEMTO). A WF1948 function generator (NF) was used for the application of tip bias potential.

F. HS-SICM Imaging in Hopping Mode

The tip was approached to the surface with v_z (0.05–7 $\mu\text{m}/\text{ms}$) until the ion current reached a set point value. The set point was set at 1–2% reduction of the “reference current” flowing when the tip was well far away from the surface (10–100 pA when the ICG method was adopted). The voltage applied to the Z-scanner yielding the set point current was recorded as the sample height at the corresponding pixel position. Here, the output from the transimpedance amplifier was high-pass filtered at 5–1000 Hz to suppress the effect of current drift on SICM imaging. Then, the pipette was retracted by a hopping distance (20 nm–50 μm within 20–50 μs , depending on the hopping amplitude, during which the pipette was moved laterally towards the next pixel position. After full retraction, the tip approaching was

performed again. Through all the HS-SICM experiments, the pipette resistance did not show a significant change, indicating no break of the pipette tip during scanning.

The value of FWHM was calculated from five height profiles of each HS-SICM image. The error of FWHM was estimated from the standard deviation.

G. Sample Preparation

(1) Glass substrate

Cover slips (Matsunami Glass, C024321) cleaned with a piranha solution for 60 min at 70 °C were used as a glass substrate.

(2) HeLa cells on glass

HeLa cells were cultured in Dulbecco’s Modified Eagle’s Medium (Gibco) supplemented with 10% fetal bovine serum. The cells were deposited on a MAS-coated glass (Matsunami Glass, S9441) and maintained in a humidified 5% CO² incubator at 37 °C until observation. Then, the culture medium was changed to phosphate buffer saline (Gibco, PBS). Then, HS-SICM measurements were performed at room temperature.

(3) HeLa cells on plastic dish

HeLa cells were seeded on plastic dishes (AS ONE, 1-8549-01) in Dulbecco’s Modified Eagle’s Medium (Gibco) supplemented with 10% fetal bovine serum. The cells were incubated at 37 °C with 5% CO² and measured by HS-SICM 3–4 days after seeding. Before HS-SICM measurements, the culture medium was changed to phosphate buffer saline (Gibco, PBS). HS-SICM measurements were performed at room temperature.

(4) Actin filaments on glass substrate

The glass surface was first coated with (3-aminopropyl) triethoxysilane (APTES; Sigma Aldrich). Then, a drop (12 μL) of actin filaments prepared according to the method [62] and diluted to 3 μM in Buffer A containing 25 mM KCl, 2 mM MgCl₂, 1 mM EGTA, 20 mM imidazole-HCl (pH7.6) was deposited to the glass surface and incubated for 15 min. Unattached actin filaments were washed out with Buffer A.

(5) Actin filaments on lipid bilayer

The mica surface was coated with lipids containing 1,2-dipalmitoyl-sn-glycero-3-phosphocholine (DPPC) and 1,2-dipalmitoyl-sn-glycero-3-phosphoethanolamine-N-(cap biotinyl) (biotin-cap-DPPE) in a weight ratio of 0.99:0.01, according to the method [63]. Partially biotinylated actin filaments in Buffer A prepared according to the method [64] were immobilized on the lipid bilayer surface through streptavidin with a low surface density. Unattached actin filaments were washed out with Buffer A.

H. FEM Simulations

We employed three-dimensional FEM simulations to study electrostatics and ionic mass transport processes in the pipette tip with ICG. In the simulation, we used the rotational symmetry along the pipette axis to reduce the simulation time. The full detail is described in SI 3. Briefly, the following set of equations were solved numerically:

$$\nabla^2 V = -\frac{F}{\varepsilon_0 \varepsilon} \sum_{j=1}^2 Z_j c_j \quad (4)$$

$$\mathbf{J}_j = -D_j(c) \nabla c_j - \frac{F Z_j c_j D_j(c)}{RT} \nabla V, \quad (5)$$

$$\nabla \cdot \mathbf{J}_j = 0$$

$$\mathbf{n} \cdot \nabla \phi = \frac{-\sigma}{\varepsilon_0 \varepsilon}. \quad (6)$$

The Poisson equation Eq. (4) describes the electrostatic potential V and electric field with a spatial charge distribution in a continuous medium of permittivity ε containing the ions j of concentration c_j and charge Z_j . F and ε_0 are the Faraday constant and the vacuum permittivity, respectively. We assume that the movement of the tip is sufficiently slow not to agitate the solution, and thus, the time-independent Nernst–Planck equation, Eq. (5), holds, where \mathbf{J}_j , $D_j(c)$, R and T are the ion flux concentration of j , concentration-dependent diffusion constant of j , gas constant, and temperature in kelvin, respectively. This equation describes the diffusion and migration of the ions. The boundary condition for Eq. (5) is determined so that a zero flux or constant concentration condition is satisfied. On the other hand, the boundary conditions of

Eq. (4) are given so that a fixed potential or the spatial distribution of the surface charge σ , as described in Eq. (6), holds. In Eq. (6), \mathbf{n} represents the surface normal vector.

SUPPLEMENTARY MATERIALS

The following data are available as [Supplementary material](#): performance of XYZ-Scanner, current noise in our SICM system, finite-element simulation, dynamic response of measured ion current with and without use of ICG method, simulated approach curves obtained with and without the use of ICG method, current noise caused by capacitive couplings between Z-scanner and signal line of current detection, high-speed SICM imagings of grating samples and peripheral edge of HeLa cells, HS-SICM images of microvilli dynamics of HeLa cell ([Movie 1](#)), and HS-SICM images of polymers ([Movie 2](#)).

ACKNOWLEDGMENTS

This work was supported by a grant of JST SENTAN (JPMJSN16B4 to S.W.), Grant for Young Scientists from Hokuriku Bank (to S.W.), JSPS Grant-in-Aid for Young Scientists (B) (JP26790048 to S.W.), JSPS Grant-in-Aid for Young Scientists (A) (JP17H04818 to S.W.), JSPS Grant-in-Aid for Scientific Research on Innovative Areas (JP16H00799 to S.W.) and JSPS Grant-in-Aid for Challenging Exploratory Research (JP18K19018 to S.W.) and JSPS Grant-in-Aid for Scientific Research (S) (JP17H06121 and JP24227005 to T.A.). This work was also supported by a Kanazawa University CHOZEN project and World Premier International Research Center Initiative (WPI), MEXT, Japan.

-
- [1] P. Hansma, J. Cleveland, M. Radmacher, D. Walters, P. Hillner, M. Bezanilla, M. Fritz, D. Vie, H. Hansma, C. Prater, J. Massie, L. Fukunaga, J. Gurley, and V. Elings, Tapping mode atomic force microscopy in liquids, *Applied Physics Letters* **64**, 1738 (1994).
 - [2] S. Zhang, S.-J. Cho, K. Busuttil, C. Wang, F. Besenbacher, and M. Dong, Scanning ion conductance microscopy studies of amyloid fibrils at nanoscale, *Nanoscale* **4**, 3105 (2012).
 - [3] T. Ushiki, M. Nakajima, M. Choi, S.-J. Cho, and F. Iwata, Scanning ion conductance microscopy for imaging biological samples in liquid: A comparative study with atomic force microscopy and scanning electron microscopy, *Micron* **43**, 1390 (2012).
 - [4] T. Ando, High-speed atomic force microscopy and its future prospects, *Biophysical reviews* **10**, 285 (2018).
 - [5] J. Seifert, J. Rheinlaender, P. Novak, Y. E. Korchev, and T. E. Schäffer, Comparison of atomic force microscopy and scanning ion conductance microscopy for live cell imaging, *Langmuir* **31**, 6807 (2015).
 - [6] P. Hansma, B. Drake, O. Marti, S. Gould, and C. Prater, The scanning ion-conductance microscope, *Science* **243**, 641 (1989).
 - [7] S. Del Linz, E. Willman, M. Caldwell, D. Klenerman, A. Fernández, and G. Moss, Contact-free scanning and imaging with the scanning ion conductance microscope, *Analytical chemistry* **86**, 2353 (2014).
 - [8] D. Thatenhorst, J. Rheinlaender, T. E. Schäffer, I. D. Dietzel, and P. Happel, Effect of sample slope on image formation in scanning ion conductance microscopy, *Analytical chemistry* **86**, 9838 (2014).
 - [9] L. Steinbock, J. Steinbock, and A. Radenovic, Controllable shrinking and shaping of glass nanocapillaries under electron irradiation, *Nano letters* **13**, 1717 (2013).
 - [10] X. Xu, C. Li, Y. Zhou, and Y. Jin, Controllable shrinking of glass capillary nanopores down to sub-10 nm by wet-chemical silanization for signal-enhanced dna translocation, *ACS sensors* **2**, 1452 (2017).
 - [11] J. Y. Sze, S. Kumar, A. P. Ivanov, S.-H. Oh, and J. B. Edl, Fine tuning of nanopipettes using atomic layer

- deposition for single molecule sensing, *Analyst* **140**, 4828 (2015).
- [12] D. Pastré, H. Iwamoto, J. Liu, G. Szabo, and Z. Shao, Characterization of ac mode scanning ion-conductance microscopy, *Ultramicroscopy* **90**, 13 (2001).
- [13] P. Li, L. Liu, Y. Wang, Y. Yang, C. Zhang, and G. Li, Phase modulation mode of scanning ion conductance microscopy, *Applied Physics Letters* **105**, 053113 (2014).
- [14] P. Li, L. Liu, Y. Yang, L. Zhou, D. Wang, Y. Wang, and G. Li, Amplitude modulation mode of scanning ion conductance microscopy, *Journal of laboratory automation* **20**, 457 (2015).
- [15] K. McKelvey, S. L. Kinnear, D. Perry, D. Momotenko, and P. R. Unwin, Surface charge mapping with a nanopipette, *Journal of the American Chemical Society* **136**, 13735 (2014).
- [16] K. McKelvey, D. Perry, J. C. Byers, A. W. Colburn, and P. R. Unwin, Bias modulated scanning ion conductance microscopy, *Analytical chemistry* **86**, 3639 (2014).
- [17] A. Page, D. Perry, P. Young, D. Mitchell, B. G. Frenguelli, and P. R. Unwin, Fast nanoscale surface charge mapping with pulsed-potential scanning ion conductance microscopy, *Analytical Chemistry* **88**, 10854 (2016).
- [18] D. Perry, R. Al Botros, D. Momotenko, S. L. Kinnear, and P. R. Unwin, Simultaneous nanoscale surface charge and topographical mapping, *ACS nano* **9**, 7266 (2015).
- [19] D. Perry, B. Paulose Nadappuram, D. Momotenko, P. D. Voyias, A. Page, G. Tripathi, B. G. Frenguelli, and P. R. Unwin, Surface charge visualization at viable living cells, *Journal of the American Chemical Society* **138**, 3152 (2016).
- [20] L. H. Klausen, T. Fuhs, and M. Dong, Mapping surface charge density of lipid bilayers by quantitative surface conductivity microscopy, *Nature Communications* **7**, 12447 (2016).
- [21] T. Fuhs, L. H. Klausen, S. M. Sønderskov, X. Han, and M. Dong, Direct measurement of surface charge distribution in phase separating supported lipid bilayers, *Nanoscale* **10**, 4538 (2018).
- [22] M. Kang, D. Perry, C. L. Bentley, G. West, A. Page, and P. R. Unwin, Simultaneous topography and reaction flux mapping at and around electrocatalytic nanoparticles, *ACS nano* **11**, 9525 (2017).
- [23] Y. Takahashi, A. I. Shevchuk, P. Novak, B. Babakinejad, J. Macpherson, P. R. Unwin, H. Shiku, J. Gorelik, D. Klenerman, Y. E. Korchev, *et al.*, Topographical and electrochemical nanoscale imaging of living cells using voltage-switching mode scanning electrochemical microscopy, *Proceedings of the National Academy of Sciences* **109**, 11540 (2012).
- [24] A. Bruckbauer, L. Ying, A. M. Rothery, D. Zhou, A. I. Shevchuk, C. Abell, Y. E. Korchev, and D. Klenerman, Writing with dna and protein using a nanopipet for controlled delivery, *Journal of the American Chemical Society* **124**, 8810 (2002).
- [25] B. Babakinejad, P. Jönsson, A. Løppez Córdoba, P. Actis, P. Novak, Y. Takahashi, A. Shevchuk, U. Anand, P. Anand, A. Drews, A. Ferrer-Montiel, D. Klenerman, and Y. E. Korchev, Local delivery of molecules from a nanopipette for quantitative receptor mapping on live cells, *Analytical chemistry* **85**, 9333 (2013).
- [26] A. Page, M. Kang, A. Armitstead, D. Perry, and P. R. Unwin, Quantitative visualization of molecular delivery and uptake at living cells with self-referencing scanning ion conductance microscopy-scanning electrochemical microscopy, *Analytical chemistry* **89**, 3021 (2017).
- [27] Y. Takahashi, A. I. Shevchuk, P. Novak, Y. Zhang, N. Ebejer, J. V. Macpherson, P. R. Unwin, A. J. Pollard, D. Roy, C. A. Clifford, H. Shiku, T. Matsue, D. Klenerman, and Y. E. Korchev, Multifunctional nanopipettes for nanoscale chemical imaging and localized chemical delivery at surfaces and interfaces, *Angewandte Chemie International Edition* **50**, 9638 (2011).
- [28] A. Page, D. Perry, and P. R. Unwin, Multifunctional scanning ion conductance microscopy, *Proceedings of the Royal Society A: Mathematical, Physical and Engineering Sciences* **473**, 20160889 (2017).
- [29] T. Ando, T. Uchihashi, and T. Fukuma, High-speed atomic force microscopy for nano-visualization of dynamic biomolecular processes, *Progress in Surface Science* **83**, 337 (2008).
- [30] T. Ando, T. Uchihashi, and S. Scheuring, Filming biomolecular processes by high-speed atomic force microscopy, *Chemical reviews* **114**, 3120 (2014).
- [31] J. Rheinlaender and T. E. Schäffer, Image formation, resolution, and height measurement in scanning ion conductance microscopy, *Journal of Applied Physics* **105**, 094905 (2009).
- [32] Y. Korchev, M. Milovanovic, C. Bashford, D. Bennett, E. Sviderskaya, I. Vodyanoy, and M. Lab, Specialized scanning ion-conductance microscope for imaging of living cells, *Journal of microscopy* **188**, 17 (1997).
- [33] P. Novak, C. Li, A. I. Shevchuk, R. Stepanyan, M. Caldwell, S. Hughes, T. G. Smart, J. Gorelik, V. P. Ostanin, M. J. Lab, G. W. J. Moss, G. I. Frolenkov, D. Klenerman, and Y. E. Korchev, Nanoscale live-cell imaging using hopping probe ion conductance microscopy, *Nature methods* **6**, 279 (2009).
- [34] P. Novak, A. Shevchuk, P. Ruenraroengsak, M. Miragoli, A. J. Thorley, D. Klenerman, M. J. Lab, T. D. Tetley, J. Gorelik, and Y. E. Korchev, Imaging single nanoparticle interactions with human lung cells using fast ion conductance microscopy, *Nano letters* **14**, 1202 (2014).
- [35] A. I. Shevchuk, P. Novak, M. Taylor, I. A. Diakonov, A. Ziyadeh-Isleem, M. Bitoun, P. Guicheney, J. Gorelik, C. J. Merrifield, D. Klenerman, and Y. E. Korchev, An alternative mechanism of clathrin-coated pit closure revealed by ion conductance microscopy, *The Journal of cell biology* **197**, 499 (2012).
- [36] G.-E. Jung, H. Noh, Y. K. Shin, S.-J. Kahng, K. Y. Baik, H.-B. Kim, N.-J. Cho, and S.-J. Cho, Closed-loop ars mode for scanning ion conductance microscopy with improved speed and stability for live cell imaging applications, *Nanoscale* **7**, 10989 (2015).
- [37] J. Kim, S.-O. Kim, and N.-J. Cho, Alternative configuration scheme for signal amplification with scanning ion conductance microscopy, *Review of Scientific Instruments* **86**, 023706 (2015).
- [38] P. Li, L. Liu, Y. Yang, Y. Wang, and G. Li, In-phase bias modulation mode of scanning ion conductance microscopy with capacitance compensation, *IEEE Transactions on Industrial Electronics* **62**, 6508 (2015).
- [39] H. Ida, Y. Takahashi, A. Kumatani, H. Shiku, and T. Matsue, High speed scanning ion conductance mi-

- croscopy for quantitative analysis of nanoscale dynamics of microvilli, *Analytical chemistry* **89**, 6015 (2017).
- [40] S. Simeonov and T. E. Schäffer, High-speed scanning ion conductance microscopy for sub-second topography imaging of live cells, *Nanoscale* **11**, 8579 (2019).
- [41] S. Watanabe and T. Ando, High-speed xyz-nanopositioner for scanning ion conductance microscopy, *Applied Physics Letters* **111**, 113106 (2017).
- [42] J. K. Rosenstein, M. Wanunu, C. A. Merchant, M. Drndic, and K. L. Shepard, Integrated nanopore sensing platform with sub-microsecond temporal resolution, *Nature methods* **9**, 487 (2012).
- [43] R. A. Levis and J. L. Rae, The use of quartz patch pipettes for low noise single channel recording., *Biophysical journal* **65**, 1666 (1993).
- [44] J. K. Rosenstein, S. Ramakrishnan, J. Roseman, and K. L. Shepard, Single ion channel recordings with cmos-anchored lipid membranes, *Nano letters* **13**, 2682 (2013).
- [45] N. Kodera, H. Yamashita, and T. Ando, Active damping of the scanner for high-speed atomic force microscopy, *Review of scientific instruments* **76**, 053708 (2005).
- [46] M. Kageshima, S. Togo, Y. J. Li, Y. Naitoh, and Y. Sugawara, Wideband and hysteresis-free regulation of piezoelectric actuator based on induced current for high-speed scanning probe microscopy, *Review of scientific instruments* **77**, 103701 (2006).
- [47] R. W. Clarke, A. Zhukov, O. Richards, N. Johnson, V. Ostanin, and D. Klenerman, Pipette–surface interaction: Current enhancement and intrinsic force, *Journal of the American Chemical Society* **135**, 322 (2012).
- [48] M. A. Edwards, C. G. Williams, A. L. Whitworth, and P. R. Unwin, Scanning ion conductance microscopy: a model for experimentally realistic conditions and image interpretation, *Analytical chemistry* **81**, 4482 (2009).
- [49] C. Wei, A. J. Bard, and S. W. Feldberg, Current rectification at quartz nanopipet electrodes, *Analytical Chemistry* **69**, 4627 (1997).
- [50] L. Cao, W. Guo, Y. Wang, and L. Jiang, Concentration-gradient-dependent ion current rectification in charged conical nanopores, *Langmuir* **28**, 2194 (2011).
- [51] X. L. Deng, T. Takami, J. W. Son, E. J. Kang, T. Kawai, and B. H. Park, Effect of concentration gradient on ionic current rectification in polyethyleneimine modified glass nano-pipettes, *Scientific reports* **4** (2014).
- [52] L.-H. Yeh, C. Hughes, Z. Zeng, and S. Qian, Tuning ion transport and selectivity by a salt gradient in a charged nanopore, *Analytical chemistry* **86**, 2681 (2014).
- [53] M. Z. Bazant, M. S. Kilic, B. D. Storey, and A. Ajdari, Towards an understanding of induced-charge electrokinetics at large applied voltages in concentrated solutions, *Advances in colloid and interface science* **152**, 48 (2009).
- [54] D. Perry, D. Momotenko, R. A. Lazenby, M. Kang, and P. R. Unwin, Characterization of nanopipettes, *Analytical chemistry* **88**, 5523 (2016).
- [55] R. A. Robinson and R. H. Stokes, *Electrolyte solutions* (Courier Corporation, 2002).
- [56] D. E. Goldman, Potential, impedance, and rectification in membranes, *The Journal of general physiology* **27**, 37 (1943).
- [57] A. L. Hodgkin and B. Katz, The effect of sodium ions on the electrical activity of the giant axon of the squid, *The Journal of physiology* **108**, 37 (1949).
- [58] J. Gorelik, A. I. Shevchuk, G. I. Frolenkov, I. A. Diakonov, C. J. Kros, G. P. Richardson, I. Vodyanoy, C. R. Edwards, D. Klenerman, and Y. E. Korchev, Dynamic assembly of surface structures in living cells, *Proceedings of the National Academy of Sciences* **100**, 5819 (2003).
- [59] J. Rheinlaender and T. E. Schäffer, Lateral resolution and image formation in scanning ion conductance microscopy, *Analytical chemistry* **87**, 7117 (2015).
- [60] L. Dorwling-Carter, M. Aramesh, C. Forró, R. F. Tiefenauer, I. Shorubalko, J. Vörös, and T. Zambelli, Simultaneous scanning ion conductance and atomic force microscopy with a nanopore: Effect of the aperture edge on the ion current images, *Journal of Applied Physics* **124**, 174902 (2018).
- [61] Z. Leonenko, E. Finot, H. Ma, T. Dahms, and D. Cramb, Investigation of temperature-induced phase transitions in dopc and dppc phospholipid bilayers using temperature-controlled scanning force microscopy, *Biophysical journal* **86**, 3783 (2004).
- [62] T. Sakamoto, I. Amitani, E. Yokota, and T. Ando, Direct observation of processive movement by individual myosin v molecules, *Biochemical and biophysical research communications* **272**, 586 (2000).
- [63] D. Yamamoto, T. Uchihashi, N. Kodera, H. Yamashita, S. Nishikori, T. Ogura, M. Shibata, and T. Ando, High-speed atomic force microscopy techniques for observing dynamic biomolecular processes, in *Methods in enzymology*, Vol. 475 (Elsevier, 2010) pp. 541–564.
- [64] N. Kodera, D. Yamamoto, R. Ishikawa, and T. Ando, Video imaging of walking myosin v by high-speed atomic force microscopy, *Nature* **468**, 72 (2010).